AGU PUBLICATIONS

JGR

Journal of Geophysical Research: Space Physics

RESEARCH ARTICLE

10.1002/2014JA020748

Special Section:
Low-Frequency Waves in Space Plasmas

The use of the Poynting vector in interpreting ULF waves in magnetospheric waveguides

T. Elsden[1] and A. N. Wright[1]

[1]Mathematical Institute, University of St. Andrews, St. Andrews, UK

Key Points:
- The satellite position is the key in understanding the wave signature
- The Poynting vector can be used to mark the end of the driving phase
- Two observations can be fully explained by our simulations

Correspondence to:
T. Elsden,
te55@st-andrews.ac.uk

Citation:
Elsden, T., and A. N. Wright (2015), The use of the Poynting vector in interpreting ULF waves in magnetospheric waveguides, *J. Geophys. Res. Space Physics*, *120*, 166–186, doi:10.1002/2014JA020748.

Received 20 OCT 2014
Accepted 4 DEC 2014
Accepted article online 10 DEC 2014
Published online 14 JAN 2015

Abstract We numerically model ultralow frequency (ULF) waves in the magnetosphere assuming an ideal, low-β, inhomogeneous plasma waveguide. The waveguide is based on the hydromagnetic box model. We develop a novel boundary condition that drives the magnetospheric boundary by pressure perturbations, in order to simulate solar wind dynamic pressure fluctuations disturbing the magnetopause. The model is applied to observations from Cluster and Time History of Events and Macroscale Interactions during Substorms. Our model is able to reproduce similar wave signatures to those in the data, such as a unidirectional azimuthal Poynting vector, by interpreting the observations in terms of fast waveguide modes. Despite the simplicity of the model, we can shed light on the nature of these modes and the location of the energy source relative to the spacecraft. This is achieved by demonstrating that important information, such as phase shifts between components of the electric and magnetic fields and the balance of radial to azimuthal propagation of energy, may be extracted from a careful analysis of the components of the Poynting vector.

1. Introduction

Ultralow frequency (ULF) waves are a dominant feature of Earth's magnetosphere and have been studied extensively for over half a century. From a theoretical standpoint, *Southwood* [1974] and *Chen and Hasegawa* [1974] examined the coupled equations for fast and Alfvén magnetohydrodynamic (MHD) waves arising from the cold plasma equations, choosing a uniform background field $B\hat{\mathbf{z}}$ with a density variation across the field radially in $\hat{\mathbf{x}}$. The solution reveals the location of a resonance on the field line satisfying $\omega_A^2(x) = \omega^2$. These studies also showed that surface waves excited by the Kelvin-Helmholtz instability at the magnetopause can couple to a field line resonance (FLR) within the magnetosphere. These ideas were later advanced analytically to treating the magnetosphere as a cavity in the hydromagnetic box model of *Kivelson and Southwood* [1985] and implemented numerically by *Allan et al*. [1986a, 1986b] and *Lee and Lysak* [1989]. It was argued that the driving of the cavity from an external source would excite the natural fast mode frequencies of the cavity. These in turn would, at the resonance locations, couple to the Alfvén mode resulting in a FLR. More recently, large-scale MHD simulations have been performed to attempt a more realistic modeling of magnetospheric cavity modes [e.g., *Claudepierre et al*., 2009], where it is shown that these modes can be driven by solar wind dynamic pressure fluctuations.

A drawback to the cavity model is that only discrete frequencies can be obtained due to the quantization of the wave number k_y, since the cavity is treated as axisymmetric. This model was refined to the waveguide model of the magnetosphere [e.g., *Harrold and Samson*, 1992; *Wright*, 1994], treating it as open ended to account for the structure of the magnetotail. To this end, much analytical and numerical work have been done in the papers *Wright* [1994], *Wright and Rickard* [1995a], and *Rickard and Wright* [1994, 1995] as an effort to further explain the coupling between the fast and Alfvén modes.

Observationally, the field of magnetospheric ULF waves has progressed drastically with the availability of a plethora of satellite data, compared to the times when most of the underpinning theories were developed. This permits a much more detailed comparison between the theory and the observations. In this study, we retain the numerical simplicity of the waveguide model of *Rickard and Wright* [1994] while attempting to match to recent observations. Two observational cases are considered, first, that of *Clausen et al.* [2008] reporting evidence of ULF waves from Cluster data, and second, that of *Hartinger et al.* [2012], discussing a Pc5 global mode observed by the Time History of Events and Macroscale Interactions during Substorms

(THEMIS) satellite. Henceforth, for ease of reference, these papers shall be referred to as *Clausen08* and *Hartinger12*, respectively.

In the model, we employ a new driven boundary condition where the magnetopause boundary is driven with perturbations of the field-aligned magnetic field component b_z as a means to mimic driving with pressure, which *Takahashi and Ukhorskiy* [2008] suggest is the dominant driver of magnetospheric ULF waves. This differs from previous simulations where displacement was used to drive the system [e.g., *Wright and Rickard*, 1995b].

The Poynting vector components are of particular interest for interpreting the energy flow within the domain and have long been used in the analysis of ULF waves. *Junginger* [1985] provides both an analytical and numerical treatment of the time-averaged Poynting vector in a box geometry in the presence of mode coupling. This theory is supported by *Proehl et al.* [2002], where a 3-D MHD simulation shows time-averaged radial energy diverted into the resonant surface. *Cummings et al.* [1978] used the Poynting vector to identify azimuthal propagation of a Pc4 wave. *Chi and Russell* [1998] found a correlation between the time-averaged Poynting flux and phase skips, a phenomenon where the phase changes suddenly between wave packets with a near-constant frequency. As in these studies, we demonstrate how the Poynting vector can be used to interpret ULF wave signatures.

The paper is laid out in the following way: Section 2 discusses in detail the aforementioned observations as a means to motivate our modeling. Section 3 develops the theory surrounding the waveguide approach, listing the governing equations, boundary conditions, and numerical method. Sections 4 and 5 present the results from the modeling of the events from *Clausen08* and *Hartinger12*, respectively. A comparison between the papers and some final thoughts are given in section 6. Appendix A discusses in depth how the new driven boundary condition on the magnetopause affects the nodal structure and frequency.

2. Observations

2.1. Cluster Observations

We begin by considering *Clausen08*, which discusses a large-scale Pc4 pulsation observed by ground magnetometers and the Cluster satellites. Figure 1 of *Clausen08* shows a clear wave packet signature in the ground magnetometer data most prominently in the dawn sector but also visible at magnetic local time (MLT) ~14, from 13:30 to 13:42. Stations spanning longitudes from ~50°*N* to ~75°*N* also pick up the signal, showing that the event covered a large radial distance in the magnetosphere. Cluster 3 and 4 sample roughly the same set of field lines at ~8 MLT. During the event, both Cluster 3 and Cluster 4 remained relatively close to the magnetic equator, Cluster 3 between 9.6° and 14.7° magnetic latitude with Cluster 4 between −12.0° and −7.8°. In terms of radial distance, both satellites remained around ~5 R_E. *Clausen08* determined the location of the plasmapause to be at a radius of 4.1 R_E. This indicates that both satellites sit very close to the plasmapause which will be the key to their position in our modeling. The satellite data for Cluster 3 and 4 are qualitatively similar, and we reproduce the Cluster 3 data in Figure 1 (taken from Figure 3 of *Clausen08*). The left-hand panels list the three components of the magnetic field **b** (top), electric field **E** (middle), and the Poynting vector **S** (bottom) calculated from

$$\mathbf{S} = \frac{1}{\mu_0}\mathbf{E} \times \mathbf{b},$$

where the above fields are the wave or perturbation fields. We shall concentrate on the main wave packet occurring from 13:30 to 13:42. The right-hand panels display the corresponding fast Fourier transform (FFT), showing the dominant signal at 17.2 mHz for the magnetic and electric field components, with twice the frequency as expected for the Poynting vector signals. It is remarkable that the Cluster electric and magnetic field data have not been filtered, but are genuinely coherent oscillations with a well-defined natural frequency. Considering the components, comparable field-aligned and azimuthal magnetic field perturbations of around 1 nT are observed, with negligible radial signal. We note that the growth period of the perturbation is approximately four periods (estimated from the b_z data; this will become important for modeling in terms of how long to drive the system). For the electric field we see a strong radial component, a small azimuthal component, and negligible field-aligned variation. The Poynting vector calculated from these components has an oscillatory field-aligned signature with no preferred direction showing equal energy transfer between the Northern and Southern Hemispheres. Perhaps the most interesting feature, is the azimuthal Poynting vector signature showing a purely unidirectional flow of energy into the tail. This feature

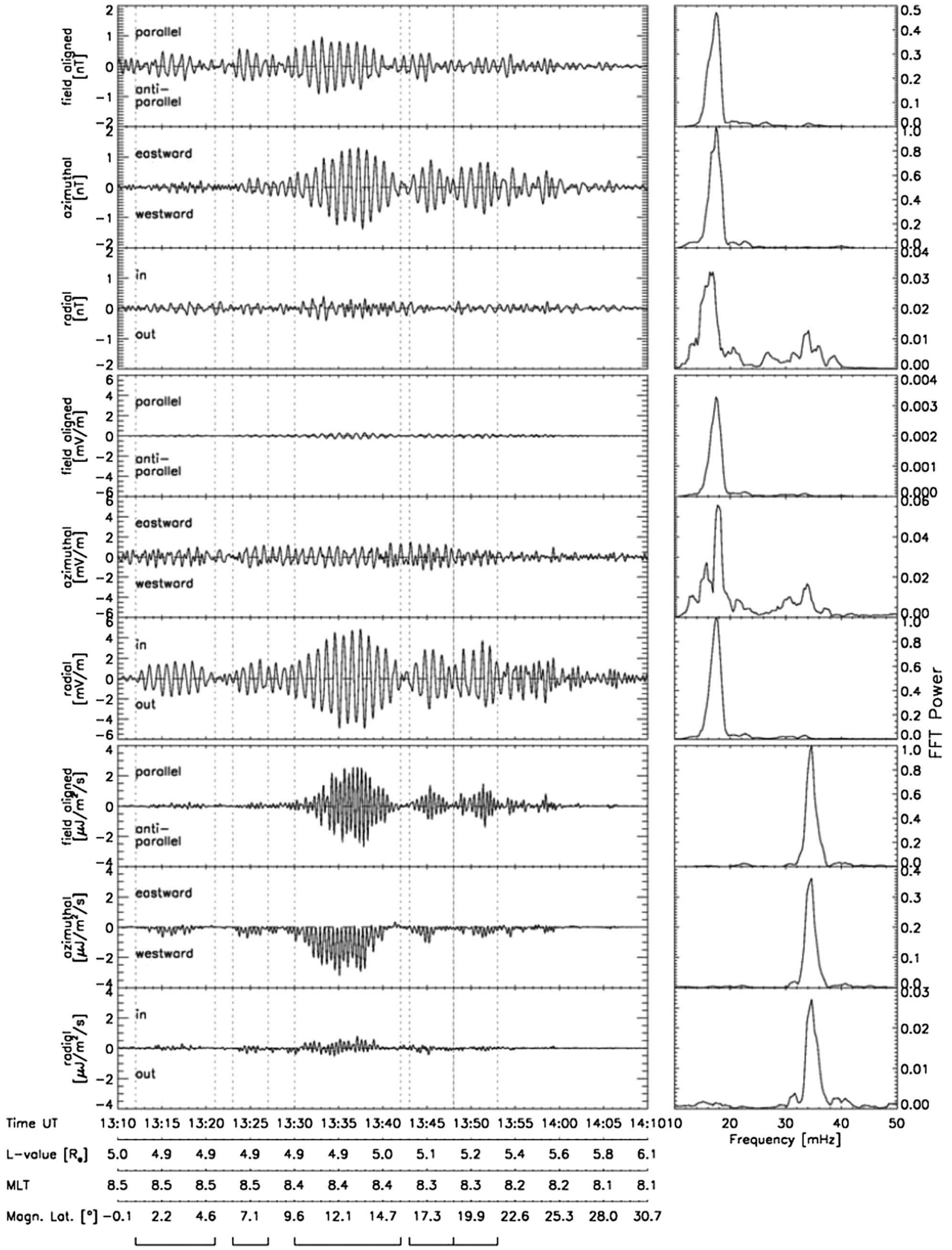

Figure 1. Reproduction of Figure 3 from *Clausen08* displaying data from the Cluster 3 satellite. (left) The three components of the magnetic field (top three panels), electric field (middle), and the Poynting vector (bottom). On the right are given the corresponding fast Fourier transform powers.

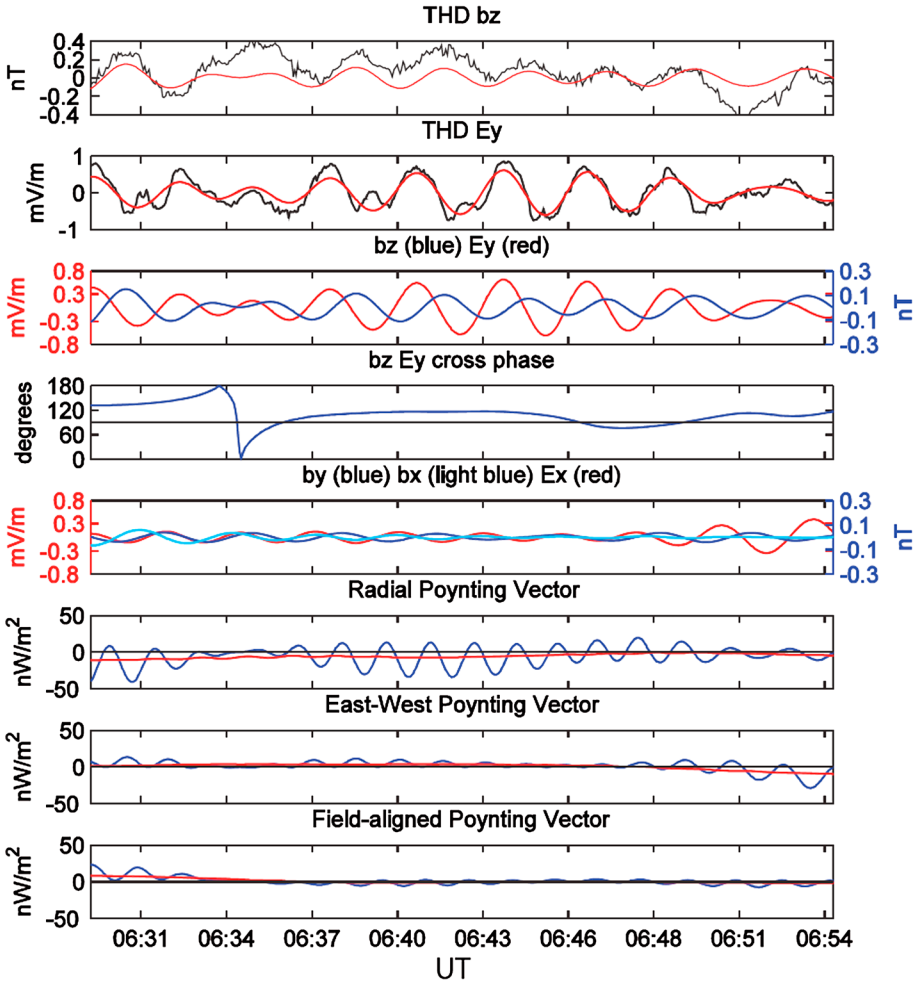

Figure 2. Reproduction of Figure 7 from *Hartinger et al.* [2012], showing satellite data from THD.

will be examined in detail in our simulations. As expected from a negligible radial magnetic field and small azimuthal electric field, there is only a small radial Poynting vector signature.

2.2. THEMIS Observations

The second observation that we consider was reported by *Hartinger12*. In this paper the authors discuss the observation of a global mode, described as "standing fast mode waves trapped between different magnetospheric boundaries." Spacecraft data from THEMIS is presented along with data from ground magnetometer stations. THEMIS consists of five satellites THA–THE, that in this case were able to observe solar wind, magnetosheath, magnetospheric, and plasmaspheric plasma. The dominant driver in this case is broadband fluctuations of solar wind dynamic pressure. The location of the plasmapause is estimated at ~7 R_E, while the dawn magnetopause is at a radial distance of ~17 R_E.

The main component results that we explain are given in Figure 7 of *Hartinger12*, and reproduced here as our Figure 2. The components are given in field-aligned coordinates for the THD spacecraft, with z being the field-aligned component, y positive eastward, and x radially outward. THD is situated at an L value of ~8.5 and MLT ~6 h, and is hence just on the magnetospheric side of the plasmapause on the dawn flank. Furthermore, THD lies within 1 R_E of the magnetic equator. The components shown in Figure 2 are band-pass filtered between 5 mHz and 8 mHz in order to isolate the global mode frequency of 6.5 mHz. Strong components b_z and E_y are observed as shown in the first and second panels (along with the high-pass-filtered data, $>$ 0.5 mHz), with weak b_x, b_y, and E_x shown together in the fifth panel. It is expected to see weak b_x and b_y components for the satellite location, close to the magnetic equator since assuming a fundamental field line structure in the z direction, these components have a node here. The Poynting vector signal composed from the magnetic and electric field components has a strong radial component which is predominantly

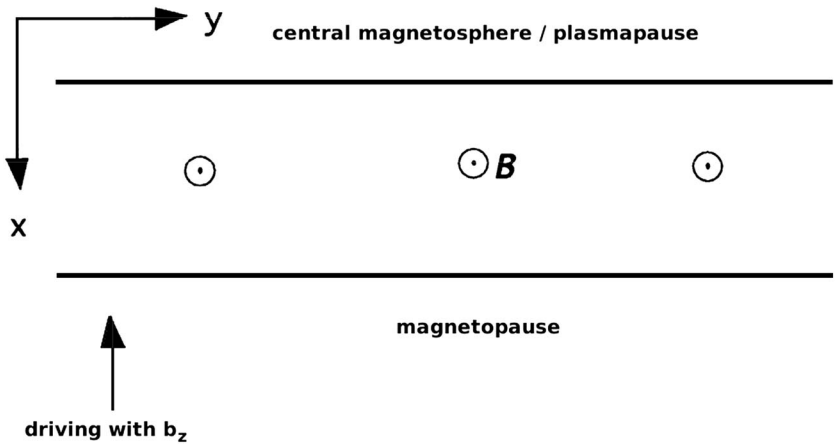

Figure 3. Magnetospheric waveguide geometry. Moving in *y* corresponds to azimuthal propagation around the dusk flank, and the driving region indicated can either model noon or flank driving.

inward, recovering to a more back and forth signal toward the end of the event. There is a very slight positive azimuthal Poynting vector signal, with a negligible field-aligned component as expected by the near equatorial position. These Poynting vector signatures are very different from those of Cluster, shown in Figure 1, and will be used to learn about the nature and location of the source of wave energy.

2.3. Observation Selection and Modeling Goals

The event outlined in *Clausen08* was selected for modeling mainly due to the Poynting vector signature showing purely tailward propagation of energy. The second event described by *Hartinger12* was chosen as a contrast to the Cluster observation in order to compare the two different signatures. The reported global mode shows very little azimuthal Poynting vector with a strong radial Poynting vector, oppositely to the Cluster event. Our goal in modeling the data is to match to the main features of the displayed components and to answer questions such as the following: What type of driving produces the tailward Poynting vector signal? How is the satellite position related to this signature and to all of the components? Can the differences in the signals be explained purely by satellite position? How can the Poynting vector be used to interpret ULF waves?

3. Model

We model the flank of the magnetosphere using a waveguide in a Cartesian system, where $\hat{\mathbf{x}}$ points radially outward, $\hat{\mathbf{y}}$ is the azimuthal coordinate around the Earth, and $\hat{\mathbf{z}}$ is field aligned, assuming a uniform background field $\mathbf{B} = B_0\hat{\mathbf{z}}$. This is in a similar fashion to the hydromagnetic box model of *Kivelson and Southwood* [1986]. A schematic of the model is given in Figure 3. In order to model a waveguide rather than a cavity, we assume an infinite length in the $\hat{\mathbf{y}}$ direction. In practice this condition is realized by ensuring that the guide is long enough such that over the course of the simulation, no disturbances reach the far boundary in *y*. The density ρ, is taken to be a function of *x* only, such that the Alfvén speed varies with radius. We assume a cold (low β), ideal plasma that has perfectly reflecting boundaries in *x* and *z*, except over the driven portion of the magnetopause. The inner boundary in *x* is assumed to be the plasmapause with the outer boundary being the magnetopause. In *z*, a fundamental standing mode structure is assumed with nodes of **u** (velocity) at the ionospheric ends of the field lines. Hence, we only need to consider a fundamental k_z Fourier mode dependence. Choosing the magnetic equator to be situated at $z = 0$, we let $u_x, u_y, b_z \sim \cos(k_z z)$, and $b_x, b_y \sim \sin(k_z z)$. Working from the equations of induction and motion, our system is then given by the dimensionless equations

$$\frac{\partial b_x}{\partial t} = -k_z u_x, \tag{1}$$

$$\frac{\partial b_y}{\partial t} = -k_z u_y, \tag{2}$$

$$\frac{\partial b_z}{\partial t} = -\left(\frac{\partial u_x}{\partial x} + \frac{\partial u_y}{\partial y}\right), \tag{3}$$

$$\frac{\partial u_x}{\partial t} = \frac{1}{\rho}\left(k_z b_x - \frac{\partial b_z}{\partial x}\right), \tag{4}$$

$$\frac{\partial u_y}{\partial t} = \frac{1}{\rho}\left(k_z b_y - \frac{\partial b_z}{\partial y}\right). \tag{5}$$

where we have normalized the magnetic field by the equilibrium magnetic field strength B_0, the density by $\rho(0)$ (at the plasmapause), and length by the width of the waveguide in x [see *Wright and Rickard*, 1995b, equations (1a)–(1e)].

The variation of the Alfvén speed with radius is given by the piecewise function

$$V_A(x) = 1 - \frac{x}{x_0},\ 0 < x \le x_c \tag{6}$$

$$V_A(x) = \frac{x_0\left(1 - \frac{x_c}{x_0}\right)^3\left(1 - x_c\right)}{\left(x_0 - 2x_c + 1\right)\left(1 - x_c\right) - \left(1 - x\right)^2},\ x_c < x < 1 \tag{7}$$

as in *Wright and Rickard* [1995b]. The point x_c defines the position where the profile switches, and x_0 defines the gradient of the profile. The above profile has the advantage that in the region $0 < x \le x_c$, the Alfvén speed is linear in x, and hence the phase-mixing length is independent of x. This allows for efficient computation by minimizing overresolution in the domain.

To integrate the system of equations given by (1)–(5) we use a leapfrog-trapezoidal algorithm, the details of which are outlined in *Rickard and Wright* [1994] (equations (13)–(15)). The grid is of length 1 (10 R_E) in the radial ($\hat{\mathbf{x}}$) direction from $x = 0 \rightarrow 1$ and 10 (100 R_E) in the azimuthal ($\hat{\mathbf{y}}$) direction from $y = 0 \rightarrow 10$. As mentioned previously, this length in y is chosen such that a disturbance will not reach the far boundary. The assumption of perfectly reflecting boundary conditions in x is accomplished by setting u_x and b_x to be zero at the inner radial boundary. We impose a symmetry condition on the $y = 0$ boundary which models the center of the driven section of the magnetopause. This could correspond to the subsolar point for symmetric dayside driving, or the flank depending upon the driving mechanism and prevailing conditions. This is realized by setting u_y and b_y to zero on this boundary. Two hundred grid points are taken in both the x and y dimensions with a time step of $\Delta t = 0.001$ (0.027 s). We ensure that the CFL condition is satisfied and the phase-mixing length resolved over the course of the simulation [*Mann et al.*, 1995; *Rickard and Wright*, 1994]. For the simulations reported in this paper, energy conservation was tested and was met to one part in 10^5 or better.

In order to drive the system, we prescribe a time-dependent profile to the field-aligned magnetic field perturbation b_z over a portion of the outer x boundary (magnetopause). We tailor this to the observation in question (see sections 4.1 and 5.1 for details). This mimics driving with pressure which is posited as the dominant driver of magnetospheric ULF waves [*Takahashi and Ukhorskiy*, 2008]. Driving in this way is different to previous works in this area by *Rickard and Wright* [1994], *Wright and Rickard* [1995b], where the system is driven by a prescribed displacement in the x direction, ξ_x. Driving with displacement simulates a node of u_x at the outer boundary, which together with a node of u_x at the inner boundary would imply that the fundamental is a half wavelength radial mode. However, changing to drive with b_z simulates a node of b_z at the outer boundary (see Appendix A) and hence an antinode of u_x. This implies that the radial fundamental for the new driving regime is a quarter wavelength mode. Adopting such a boundary condition is in agreement with *Mann et al.* [1999], who suggested that overreflected waveguide modes believed to drive discrete FLRs are more accurately modeled by such a boundary condition. They also noted that having a fundamental quarter wavelength mode can help to lower the natural waveguide eigenfrequencies to just a few mHz without changing the magnetospheric plasma density to unrealistic higher values. *Claudepierre et al.* [2009] also came across this problem in their simulation looking at magnetospheric cavity modes driven by solar wind dynamic pressure fluctuations. They found that adopting a quarter wavelength mode would much better suit the frequencies for the cavity mode.

In the following two sections we choose simulation parameters appropriate to the Cluster and THEMIS events described in section 2. We then experiment with driving conditions and satellite locations in an effort to reproduce notable signatures in the observations.

4. Cluster Modeling

4.1. Tailoring the Model

In order to model the Cluster observations we use specific input parameters given in *Clausen08*. Figure 10 from their paper displays a model of how the fundamental field line frequency will vary with L shell. As mentioned above, we take the inner boundary of the waveguide to be the plasmapause at ~4 R_E and allow a radial extent (in x) of 10 R_E to the magnetopause at ~14 R_E. Using their Figure 10, we determine that the Alfvén frequency varies from ~12 mHz at the plasmapause to ~5 mHz at the magnetopause. Assuming that the Alfvén speed is proportional to the Alfvén frequency, this allows the Alfvén speed profile to be scaled to match this frequency change. We note that these frequencies are a little high for typical fundamental Alfvén modes, probably due to lower plasma densities than normal which have elevated the normal Pc5 frequencies to the Pc4 band. Indeed, *Clausen08* suggest that it is due to the natural frequencies in this event matching the frequency of waves associated with backstreaming ions at the bow shock that the lowest-frequency modes of the magnetosphere can be excited effectively by this method [*Le and Russell*, 1996].

The system is driven with the b_z perturbation as described in section 3, with a frequency of 17.2 mHz to match the dominant frequency in the Cluster data in Figure 1. *Le and Russell* [1996] developed a model to estimate the frequency generated by backstreaming ions at the bow shock, formulating the frequency in terms of the cone angle and the interplanetary magnetic field strength. Figure 8 from *Clausen08* shows that these parameters were relatively stable over the course of the event from 13:30 to 13:40 UT. Furthermore, even broadband frequency driving can give monochromatic signatures in a cavity or waveguide [*Wright and Rickard*, 1995a]. Both of these effects justify driving monochromatically. Our equilibrium model is chosen such that the driving frequency of 17.2 mHz is the second radial harmonic of the waveguide. Considering the radial fundamental to be a quarter wavelength mode, with the prescribed boundary conditions the second harmonic has approximately 3 times the frequency of the fundamental. This implies a fundamental frequency of ~6 mHz.

In order to choose the wave number in the field-aligned direction k_z, we again refer to the Alfvén frequencies given in Figure 10 of *Clausen08*. Through the Alfvén dispersion relation $\omega_A = k_z V_A$, k_z can be adjusted with V_A in order to match both the expected fundamental frequency profile and the full dispersion relation of fast waveguide modes. This is done in practice by solving equations (1)–(5) neglecting variations in the y direction, i.e., with $k_y = 0$, using a fourth-order Runge-Kutta method to shoot for the waveguide eigenfrequencies. From this come the finalized values for the $k_y = 0$ fast natural waveguide frequencies, the field-aligned wave number k_z and the correctly scaled Alfvén speed profile. (From this analysis we find dimensionless values of $k_z = 2.28$, $x_0 = 1.514$, and $x_c = 0.8$. To get these in terms of R_E, multiply x_0 and x_c by 10 and divide k_z by 10. The normalizing magnetic field and velocity were taken as 90 nT and 2350 km s^{-1} respectively, with an inner boundary Alfvén speed of 2107 km s^{-1}.) The theory of estimating the natural waveguide frequencies by looking at the $k_y = 0$ modes was developed by *Wright* [1994] and tested in simulations by *Rickard and Wright* [1994].

The length in the z direction is now fixed by the choice of k_z and the assumption that the modes have a fundamental structure in z. This is consistent with the observed phase shift of 180° in the azimuthal magnetic field component b_y between Cluster 3 and 4. This infers that the satellites must straddle a node of b_y, one above and one below the magnetic equator. Results from a preliminary simulation using the above input parameters show that assuming a homogeneous medium in the z direction, at a satellite location modeling that of Cluster 3 ($x = 0.05$, $y = 0.6$, and $z = 0.1$ in dimensionless units), the b_y component has too small an amplitude in comparison to b_z. The b_y component is small in the simulation due to the position of both satellites near to a node of b_y at the equator. Including an inhomegeneity in z, i.e., a z dependent density profile, would create a z dependent Alfvén speed which could shift the turning point of the mode toward the equator. The low Alfvén speed in this equatorial region tends to cause the mode's phase structure to bunch up there, as seen in Figure 12 of *Clausen08* showing the Alfvén eigenfunctions. This is important as it would cause more rapid variations closer to the equator and could hence give a better match to the observed amplitudes.

To see the effects of including such an inhomogeneity, we solve equations (1)–(5) for a fast mode in a Cartesian geometry using a Runge-Kutta fourth-order method, over the full field line length, neglecting variations of the equilibrium in the perpendicular direction and imposing a z dependence on ρ such that

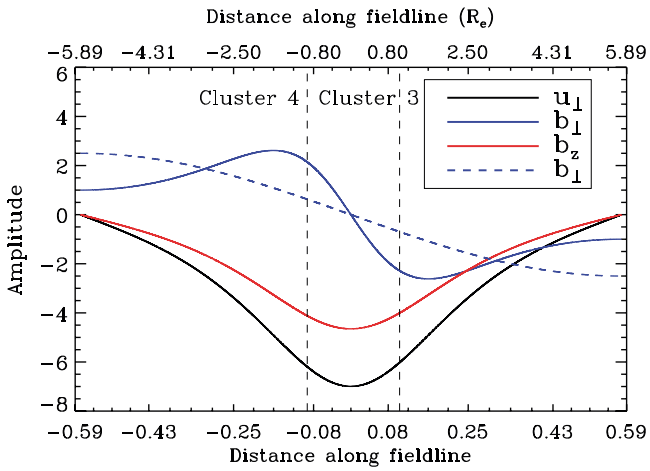

Figure 4. The parameters $u_\perp$, $b_\perp$, and b_z (solid lines) plotted against distance along the field line for a "dipole" inhomogeneity in z, with the dashed line $b_\perp$ for a homogeneous medium in z. The vertical lines show the approximate location of the Cluster satellites, approximately 2 R_E apart.

$\rho = \rho(z)$. Furthermore, we assume a dimensionless perpendicular wave number of $k_\perp = 4.71$ (which could correspond, for example, to a radial wavelength of $\lambda_x = \frac{4}{3}$ with $k_y = 0$). The increase of V_A along a field line for a dipole field is mimicked by allowing $\rho(z)$ to vary accordingly. Figure 4 gives the nodal structure of the dependent variables plotted against distance along the field line, in a similar manner to Figure 12 from *Clausen08*. The approximate locations of the Cluster satellites are denoted by the vertical dashed lines, and it is first of all evident that we see a 180° phase change in $b_\perp$ (solid blue) between them as in the observations. Second, the amplitude of $b_\perp$ changes more quickly closer to the equator than for the homogeneous case (dashed line). Indeed, at the satellite locations the amplitudes of b_z and $b_\perp$ are comparable, when V_A varies with z in accordance with the observations. The fundamental mode in z provides the desired phase shift, while including a density structure along the field produces the more rapidly changing amplitude profile close to the equator. Including a z dependence in the density increases the computing time, so we opt for a simpler approach of moving our simulation satellites in z to an equivalent phase and amplitude location, while retaining a density independent of z for computational convenience. Figure 4 shows that it is justified to move farther away from the equator along the field line closer to the amplitude peak of $b_\perp$ in our simple model. Thinking in terms of nodal structure rather than height or distance from the equator, Figure 4 demonstrates that the Cluster satellites would lie close to the antinodes of $b_\perp$. Hence, moving closer to the antinodes in our original homogeneous z structure, should simulate the amplitudes that would be found closer to the equator when there is inhomogeneity in z.

4.2. Results

Figure 5 shows the time dependence of b_z on the outer driven boundary at $x = 10\ R_E$. The system is driven for four periods of 17.2 mHz to match the observed growth phase of the b_z perturbation in the Cluster 3 data, and after four cycles the driver is switched off. The spatial dependence of b_z along the outer boundary at $x = 10\ R_E$ in the y direction is given in Figure 6. The extent of the disturbance on the magnetopause boundary, i.e., the size of the driven region, corresponds to a physical length of 5 R_E (and a full width of 10 R_E).

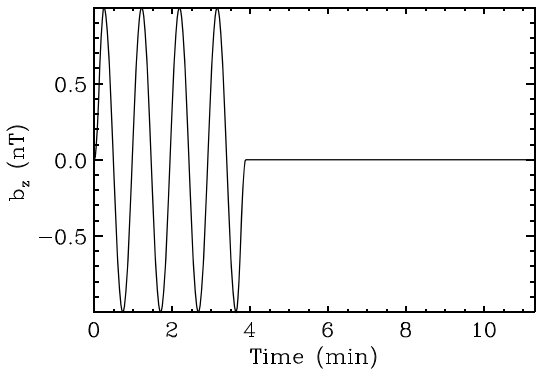

Figure 5. Temporal variation of the b_z driver on the driven boundary $x = 10\ R_E$ at $y = 0$.

The satellite position for Cluster 3 is taken to be at 4.5 R_E in x and 6 R_E in y. These are taken as approximations to the real location of the satellite and considering the geometric simplifications of our model. This corresponds to dimensionless coordinates $x = 0.05$ and $y = 0.6$, recalling that the inner boundary of the waveguide at $x = 0$ corresponds to a radial position of 4 R_E. The length of a field line in z is determined by the choice of k_z. For the given input parameters the length in z is 1.378 and hence extends from $-0.689 \rightarrow 0.689$, corresponding to a dimensional length of almost 14 R_E. The perpendicular components of the magnetic field have antinodes at the ends of

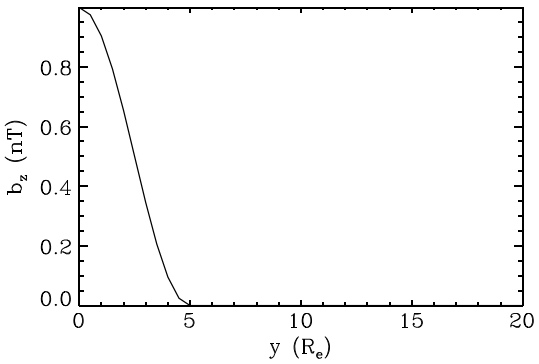

Figure 6. Spatial variation in y of b_z on the driven boundary $x = 10\ R_E$.

the field lines. As discussed above, moving toward the antinodes of $b_\perp$ should simulate the amplitudes that would be observed if an inhomegeneity in z was considered. Hence, the position in z is chosen as 0.45 approximately two thirds along the length of the field line.

Figure 7 displays the magnetic field, velocity field, and Poynting vector components from the simulation for the satellite position $x = 0.05$, $y = 0.6$, and $z = 0.45$ as discussed above. The first vertical dashed line represents the time when the driver is switched off at $t = 3.88$ min. The heightened amplitudes during driving extend past the driver switch off time by approximately the radial travel time ($t \sim 1.04$ min, shown by the second vertical dashed line), since the satellite is located close to the inner boundary. As in the observations, the field-aligned and azimuthal magnetic field components have similar amplitudes, shown in Figures 7a and 7b, respectively. Notice also how b_y falls off as soon as the driving stops (plus radial travel time) at around $t = 5$ min. The field-aligned component is persistent post driving, which is a result of driving on resonance: as we drive with the natural frequency of the second radial waveguide harmonic, no other modes are excited to the same extent, and hence we see a clear monochromatic response after the driving has stopped. The radial component b_x given in Figure 7c is small due to the position of the satellite close to the inner boundary (plasmapause), where b_x has a node.

Through the equations and the simplifications made, only the perpendicular components to the velocity remain and are shown in Figures 7d and 7e. Recall that the electric field has been eliminated in favor of the velocity field in our model. For the purpose of comparison the components may be identified as $u_x \sim E_y$ and $u_y \sim -E_x$. The position of the satellite close to the perfectly reflecting inner boundary where $u_x = 0$ causes the radial component of velocity (and E_y) to be small. The azimuthal component of velocity (and E_x) has an increased amplitude during the driven phase, but then decays in the same manner as b_y. Note the comparison to the real data here, with a strong E_x and weak E_y matching the simulation with strong u_y and weak u_x.

A diagnostic of energy flow within the system is the Poynting vector, the components of which are given in Figures 7f–7h. The field-aligned and azimuthal signatures dominate, with the radial component being weaker, as in the case of b_x and u_x, due to the near inner boundary position. The field-aligned component of **S** shows equal parallel to antiparallel transport of energy, as is expected for modes that stand in z in the absence of ionospheric dissipation. The azimuthal component matches well to the striking result from Figure 1, where we clearly see the purely tailward (positive azimuthally in our model) propagation of energy. Since the perpendicular magnetic and velocity field components have a decreased amplitude signal post driving, this feature is seen in the Poynting vector signal as well.

Clausen08 report certain phase shifts in the electric and magnetic field components at each Cluster satellite and between the satellites. First, the observations display a 180° phase shift in b_y between Cluster 3 and Cluster 4. This phase shift indicates that the modes have a fundamental standing structure in z, with Cluster 3 above the magnetic equator and Cluster 4 below. This property is clearly seen in Figure 8 (top), where the simulation position of Cluster 4 is taken to be $x = 0.05$, $y = 0.6$, and $z = -0.45$. Also present in the observations is a 90° phase shift between the field-aligned and azimuthal magnetic field components at any given satellite. Figure 8 (middle) shows the phase shift between these components at Cluster 3 and indeed matches well to the observations. Finally, *Clausen08* observe a 180° phase shift between E_x and b_z which is reproduced from the simulation in Figure 8 (bottom). As we have chosen to eliminate the electric field for the velocity field, the plot gives the negative azimuthal velocity which is associated with the radial electric field.

4.3. Discussion

Clausen08 interpret their data as a waveguide mode coupling to two FLRs. These were identified in ground magnetometer data and correspond to a fundamental mode at $L \sim 2$–3, and a second harmonic at $L \sim 8$–10.

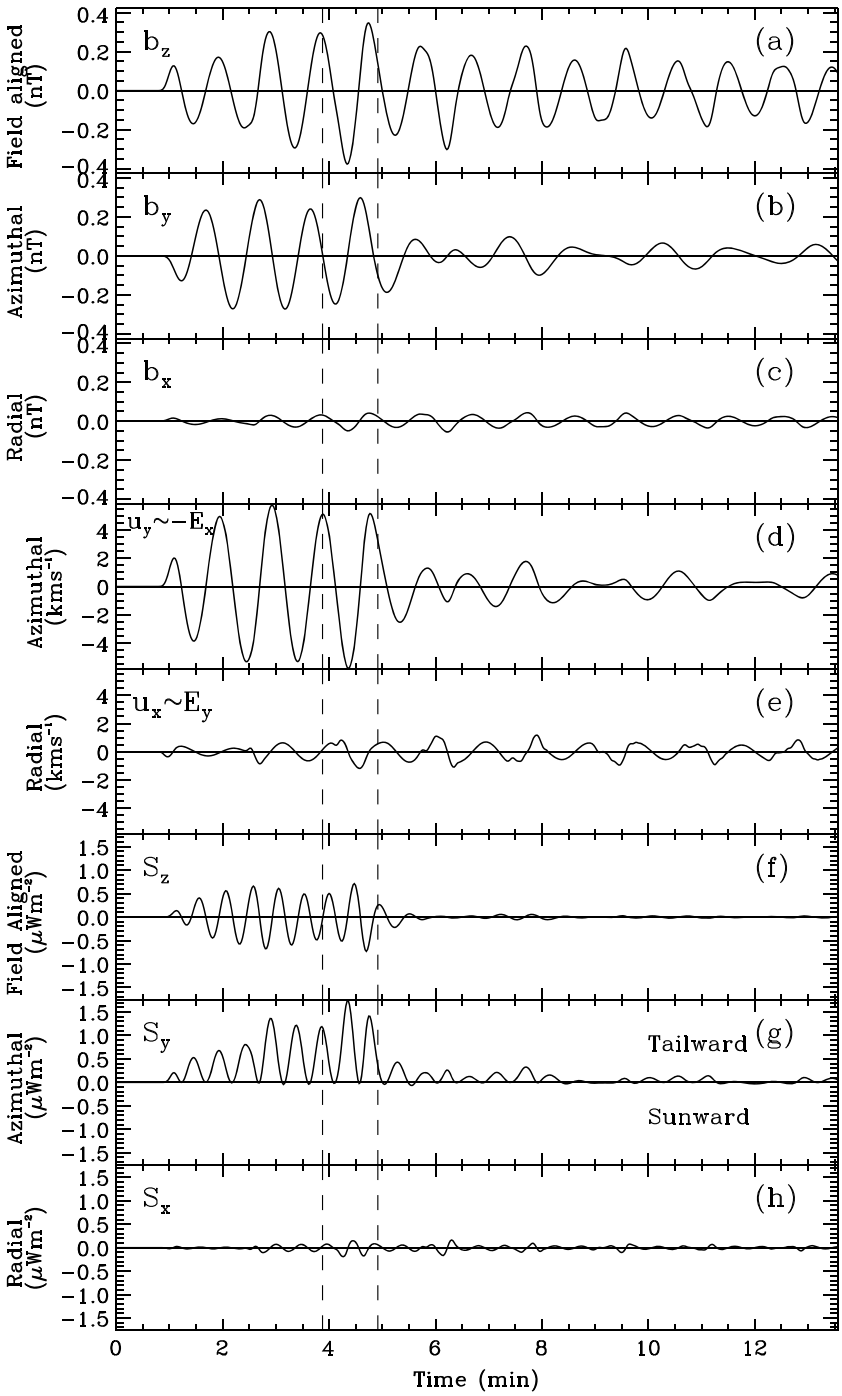

Figure 7. (a–c) Components of the magnetic field, (d and e) velocity field, and (f–h) the Poynting vector at $x = 0.05$, $y = 0.6$, and $z = 0.45$, modeling the position of Cluster 3 from *Clausen08*. The first vertical dashed line at $t = 3.88$ min is the time when the driver is switched off and the second at $t = 4.92$ min includes the radial travel time.

Note that Cluster (at $L = 5$) is not expected to observe either of the FLRs. Indeed, we suggest that the Cluster observations provide a rather clean observation of a resonantly excited waveguide mode. There are several respects in which the satellite data do not fit well with an Alfvén wave interpretation. The strong b_z component in the observations, of similar amplitude to the b_y perturbation, is not usually associated with an Alfvén wave. If a fast mode was driving an Alfvén resonance, one would expect to see persistent signals in b_y and E_x post driving until damped through ionospheric dissipation. Here, however, these components are very closely correlated with b_z. Furthermore, the expected resonance position can be estimated in the simulation

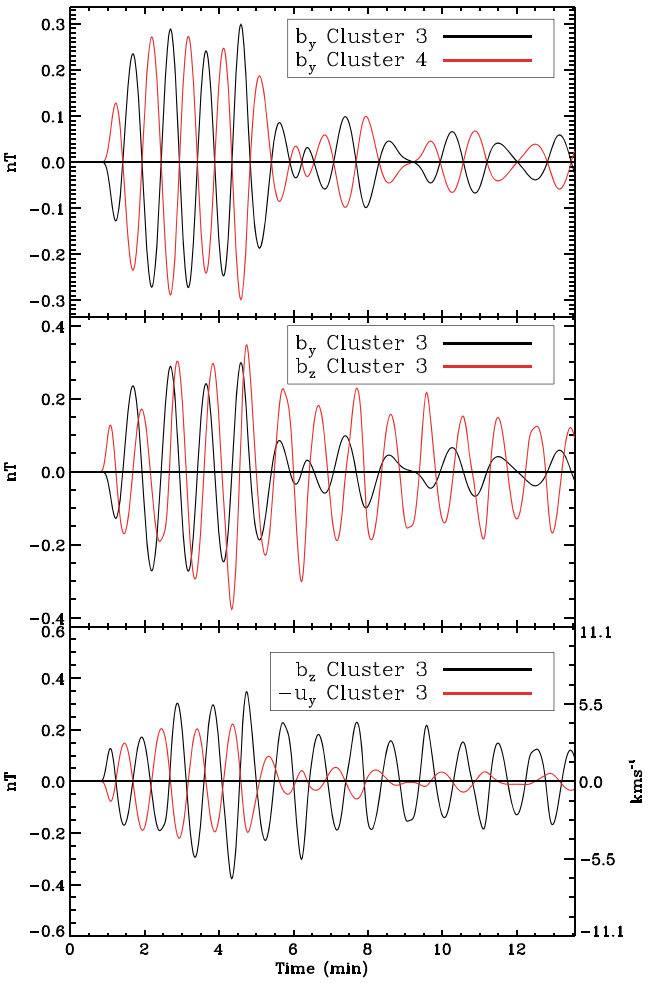

Figure 8. Simulation results matching observed phase shifts. (top) The parameter b_y from Cluster 3 (black) with b_y from Cluster 4 (red); (middle) b_y from Cluster 3 (black) with b_z from Cluster 3 (red); and (bottom) b_z from Cluster 3 (black) with $-u_y$ (E_x) from Cluster 3 (red).

assuming that a driving frequency similar to the k_y ~0 modes is responsible for the driving. As in Figure 4 from *Wright and Rickard* [1995b], we can plot the resonance position as a function of the density parameter x_0. For the given density structure the resonance position does not exist within the domain, suggesting that at no point does the Alfvén frequency at Cluster match the fast mode driving frequency. This conclusion can also be drawn from Figure 10 of *Clausen08*, where the fundamental field line frequency is plotted against radial distance. The driving frequency of 17.2 mHz does not lie within the magnetospheric portion of the plot (it is inside the plasmasphere), suggesting that this frequency will not match any field line fundamental frequency within the waveguide domain. (See the earlier comments regarding FLR locations deduced from magnetometer data.)

The simulation provides very similar results to the Cluster observations in terms of a fast waveguide mode. The main factor responsible for the form of the signal is the satellite position relative to the driving region. The purely tailward azimuthal Poynting vector signal can be explained by being tailward of the driving region. Fast mode energy enters the waveguide and the larger k_y modes will propagate downtail, while the small k_y modes will remain close to the $y = 0$ boundary. Other simulations (not shown here) demonstrate that if the satellite sits within the azimuthal extent of the driver, signals traveling sunward (negative S_y) and tailward (positive S_y) can be detected, since a fast mode source element creates a disturbance which propagates in all directions. Being farther downtail than the driven region however, only signals traveling downstream can be recorded. We believe this to be the simple explanation of the azimuthal Poynting vector signature: a downstream observation of a fast mode source.

The observed phase shifts can be explained in terms of a simple analytic solution considering a Cartesian geometry with propagation in y and a standing mode in x and z for a uniform density as an illustration. This yields the components

$$u_y \sim \cos(\omega t - k_y y)\cos(k_x x)\cos(k_z z),$$
$$b_y \sim \sin(\omega t - k_y y)\cos(k_x x)\sin(k_z z),$$
$$b_z \sim \cos(\omega t - k_y y)\cos(k_x x)\cos(k_z z).$$

It is clear that the phase shifts depicted in Figure 8 match those from the above components. The 180° phase shift between E_x and b_z at Cluster 3 or as in our model u_y and b_z being in phase, determines the unidirectionality of the azimuthal Poynting vector. Hence, a Poynting vector signature of this type will always

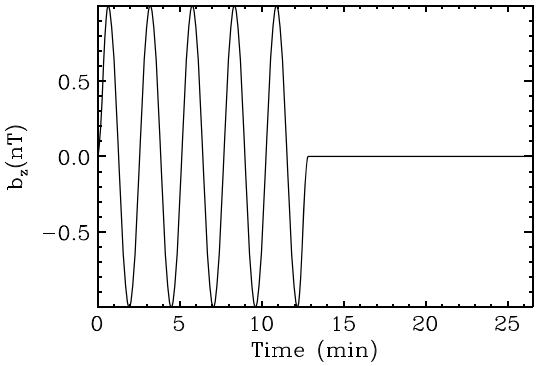

Figure 9. Temporal variation of b_z on driven boundary at $x = 10$ R_E, $y = 0$ (magnetopause).

coincide with this phase shift. The 90° phase shift between b_z and b_y again at Cluster 3 is also another signature of propagation in the y direction.

5. THEMIS Modeling

5.1. Tailoring the Model

We now adjust our model to match the situation appropriate to the THEMIS data reported in Figure 2. We take a waveguide of width 10 R_E spanning from $L \sim 7$ to $L \sim 17$, modeling from the plasmapause to the magnetopause. Using the values quoted for the Alfvén speed at $L \sim 8$ from *Hartinger12*, we take the Alfvén speed at the plasmapause, to be $V_A(0) = 1200$ km s^{-1}. This value together with the normalizing length scale of 10 R_E (the width of the waveguide) defines a time scale for the model of $T_0 = 53.1$ s. With these values, the dimensional frequency of 6.5 mHz for the global mode can be converted into a dimensionless angular frequency of $\omega = 2.1683$. As discussed in section 3 we drive the system with the b_z perturbation, assuming a quarter wavelength mode as the first harmonic in the radial direction. *Hartinger12* had difficulty resolving the radial structure in agreement with the observed frequencies. We choose to treat the observed frequency as a second radial harmonic which gives a realistic fundamental natural waveguide frequency value. A fundamental mode structure is assumed in the z direction, taking $k_z = \pi/2$. The values of x_0 and x_c, parameters determining the density profile given in equations (6) and (7), are 1.098 and 0.8, respectively.

We model the THD observations such that a comparison can be made to the component plots of Figure 2. THD, along with the other satellites within the magnetosphere, is assumed to be in approximate radial alignment with the center of the energy source region on the driven magnetopause. Hence, we are assuming that the magnetopause is driven on the flanks in this event, rather than at the subsolar point as in the Cluster event. The reasons for this assumption are apparent from the simulation results and will be discussed in section 5.3. Hence, the satellite is placed in the simulation domain close to the $y = 0$ boundary, within the azimuthal extent of the driving region, at $y = 1$ R_E. Note that $y = 0$ in this event corresponds to an MLT of 6 h. The x position is taken to be $x = 2$ R_E, modeling the location of THD approximately 2 R_E outside of the plasmapause. The location in z near to the magnetic equator is chosen as $z = 1$ R_E.

5.2. Results

To simulate the observed signal, rather than driving with a broadband signal and filtering the data for the 6.5 mHz signal, the system is driven directly with the global mode frequency. We choose to drive with five cycles of b_z, in order to match the number of observed driving periods in Figure 2. The magnetopause boundary is driven over an extent of 5 R_E (0.5 in dimensionless units). The temporal and spatial variation of the driver are shown in Figures 9 and 10.

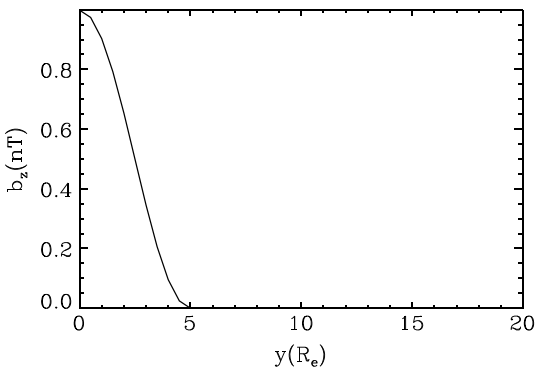

Figure 10. Spatial variation of b_z on driven boundary at $x = 10$ R_E.

The components of the magnetic field, velocity field, and Poynting vector from the simulation at a satellite with position $x = 2$ R_E, $y = 1$ R_E, and $z = 1$ R_E modeling the location of THD are displayed in Figure 11. The first vertical dashed line demarcates the time when the driver is switched off, at $t = 12.82$ min, with the second adding on the radial travel time of ~ 2.03 min. This second line matches well to the amplitude decrease of the components. The small amplitudes of b_y and b_x in Figures 11b and 11c can be attributed to the close proximity to the magnetic equator, where these components have nodes. The field-aligned magnetic signature in

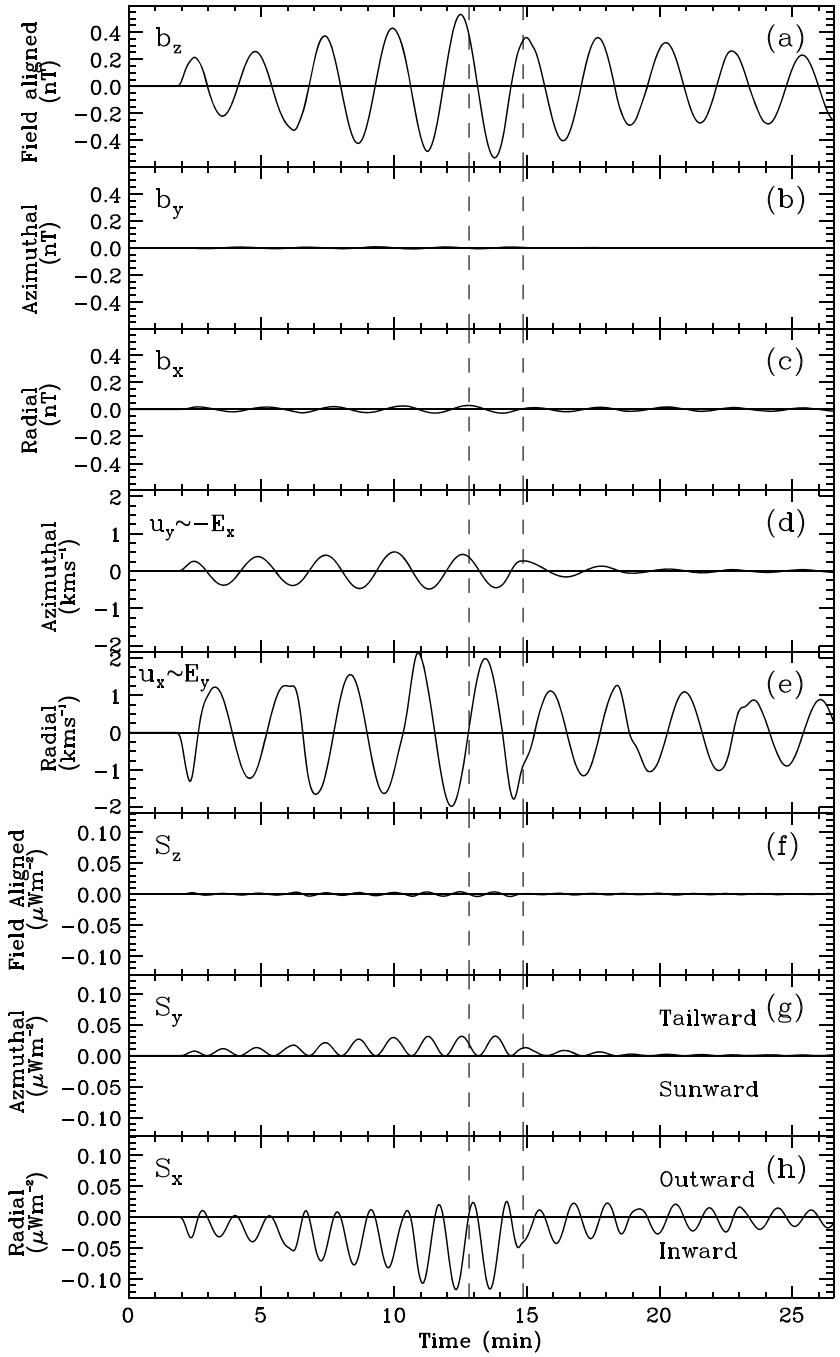

Figure 11. (a–c) Components of the magnetic field, (d and e) velocity field and (f–h) the Poynting vector at $x = 2\ R_E$, $y = 1\ R_E$, and $z = 1\ R_E$, modeling the position of THD from *Hartinger12*. The vertical dashed lines mark, first, the time where the driver is turned off, at $t = 12.82$ min and, second, the radial travel time of $t = 2.03$ min added to the driver switch off time.

Figure 11a dominates with increasing amplitude over the driving period, changing to a decaying amplitude signal post driving. The persistence of a coherent monochromatic signal once the driver has been switched off is due to the system being driven at the second radial harmonic frequency. This precludes the appearance of other frequency modes in the data and therefore post driving, the waveguide reverberates with this natural frequency. Overall, the magnetic field component results from the numerical model compare favorably to the components shown in the third and fifth panels of Figure 2. For the velocity field, Figure 11e shows a strong radial component corresponding to the negative of the azimuthal electric field (E_y in

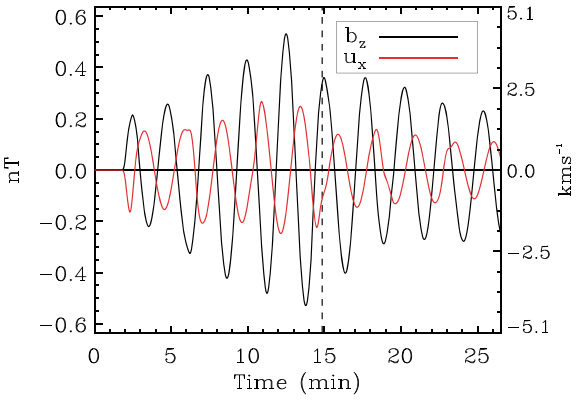

Figure 12. Phase comparison of b_z and u_x at $x = 2\ R_E$, $y = 1\ R_E$, and $z = 1\ R_E$. The dotted line indicates the time when the driver is switched off with the addition of the radial travel time, giving $t = 14.85$ min.

Figure 2, second panel). The signal is similar in structure to the field-aligned magnetic field, with increasing amplitude during driving leading to a gently decaying oscillation post driving. The azimuthal component in Figure 11d is small in good agreement with the radial electric field (E_x) from the real data. Finally, for the Poynting vector components, the nodes of b_x and b_y at the magnetic equator translate to a node of S_z, resulting in a negligible field-aligned component shown in Figure 11f. Figure 11g gives the azimuthal Poynting vector, which is small in amplitude and marginally tailward (positive) during the driving period. Post driving, the signal decays rapidly. The radial Poynting vector given in Figure 11h is almost entirely inward until the driver is switched off, at which point the signal recovers to a back and forth flow of energy.

A phase shift of 90° between b_z and E_y is expected for a radially standing global mode [*Waters et al.*, 2002]. Figure 12 shows the time signals of b_z and u_x (E_y) at the position of THD, with the vertical dashed line marking the radial travel time added to the driver switch off time. Up until this point (during driving), b_z and u_x have a phase difference between 90° and 180°. Post driving, a very clear change in the phase occurs, with the signals being almost exactly 90° out of phase.

5.3. Discussion

As with the previous study of *Clausen08* we show that the observational results of *Hartinger12* can be reproduced accurately by our numerical simulation. The key to a good match is identifying an appropriate satellite location. The small azimuthal Poynting vector signal, in contrast to the *Clausen08* study, tells us that THD must have an azimuthal location that is close to the middle of the driven section of the magnetopause. This is a means of inferring the source location in reference to the satellite position, i.e., the center of the energy source lies approximately on the same flank meridian as THD.

The observed signal from *Hartinger12* is believed to be a global mode, standing in the radial direction. The overall inward S_x shown in the sixth panel of Figure 2 suggests that energy is lost either downtail or through the inner boundary at the plasmapause during the driving phase. The azimuthal Poynting vector signal is small in comparison to the radial component and would at first sight suggest that the energy does not leak out down the tail. The same structure is seen in the simulation; however, with a slightly more inward radial Poynting vector, yet the simulation allows for no energy to leak out of the inner boundary (which is treated as perfectly reflecting) or to be coupled to a FLR earthward of the spacecraft. This can be confirmed by considering the energy continuity equation

$$\frac{\partial W}{\partial t} + \nabla \cdot \mathbf{S} = 0,$$

where W represents the energy density. Consider a small area in the computational domain, from 0 to a in y and from 0 to b in x. Integrating in space over this area yields

$$\frac{\mathrm{d}}{\mathrm{d}t}\int_0^a\int_0^b W\mathrm{d}x\mathrm{d}y + \int_0^a S_x\mathrm{d}y + \int_0^b S_y\mathrm{d}x = 0.$$

Performing the above calculation for the duration of the run for the THEMIS simulation with $a = 0.1$ and $b = 0.2$ (given in dimensionless units matching the y and x locations of THD), we find that the first term accounts for ~1% of the sum. This results in the inward flow of energy being balanced by the flow of energy downtail, despite a cursory inspection of the data suggesting the net inward flow of energy may be balanced by the increasing wave amplitude during driving. This confirms that a net inward S_x can result without the need for a leaky inner boundary or energy loss to an FLR.

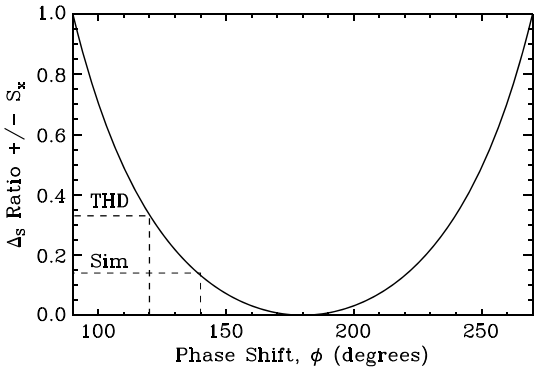

Figure 13. The absolute value of the ratio of maximum inward to maximum outward radial Poynting vector Δ_s, against the phase ϕ, by which b_z leads u_x. The dashed lines represent the observed phase shifts and ratios from THD and the simulation, labeled "THD" and "Sim," respectively.

The phase comparison between b_z and u_x shown in Figure 12 highlights the difference between the driving and post driving phases. During the driving phase, there is an overall inward propagation of energy as evident from the shape of the radial Poynting vector S_x [*Chi and Russell*, 1998], and hence the phases do not adhere to the radial standing mode phase regime of b_z and u_x being 90° out of phase but instead are phase shifted by between 90° and 180°. Post driving, the phase shift changes to 90° and S_x returns to an equally inward and outward signal. To try to better understand the relation between the inward radial Poynting vector signal S_x and the observed phase shifts, we consider the simplest means of describing the signals in Figure 12: two sinusoidal curves with a phase shift, expressed as

$$\frac{u_x}{u_0} = \sin(\omega t),$$
$$\frac{b_z}{b_0} = \sin(\omega t + \phi),$$

where ϕ is the phase by which b_z leads u_x. Constructing S_x yields

$$S_x = u_x b_z,$$
$$\frac{S_x}{u_0 b_0} = \frac{1}{2}\cos\phi + \frac{1}{2}\left(\sin\phi\,\sin(2\omega t) - \cos\phi\,\cos(2\omega t)\right).$$

The second term on the right-hand side can be expressed as a single sinusoid which gives

$$\frac{S_x}{u_0 b_0} = \frac{1}{2}\cos\phi + \frac{1}{2}\cos(2\omega t + \phi_1),$$

where ϕ_1 is the new phase dependent on ϕ. *Chi and Russell* [1998] give plots of S_x for the two limits $\phi = 0$ (propagating) and $\phi = \pi/2$ (standing). The above equation is valid for intermediate cases too. For a net inward energy flow, $90° < \phi < 270°$. The quantity important for linking the shape of the radial Poynting vector S_x to the phase shift is the ratio of positive to negative S_x signal. This is defined as the absolute value of the maximum outward S_x to the maximum inward S_x:

$$\Delta_s = \left|\frac{\cos\phi + 1}{\cos\phi - 1}\right|.$$

Figure 13 displays how this ratio Δ_s varies with the phase shift ϕ. It is clear that there is a unique relationship between these quantities, such that a specific phase shift determines the value of Δ_s. A ratio of 1.0 corresponds to b_z and u_x being 90° (or 270°) out of phase, which is in keeping with the idea of a standing radial mode with equal inward and outward propagation. A ratio of 0 implies a phase shift of 180°, consistent with a purely inward radial Poynting vector. The dashed lines represent the observed phase shifts and ratios from the observation (labeled "THD") and the simulation (labeled "Sim"). For the observation, these can be obtained from Figure 2, with the fourth panel showing a phase shift of 120° during driving, with a ratio estimated from the sixth panel of $\frac{1}{3}$. This is consistent with the predicted values in Figure 13. For the simulation, the ratio and phase shift during driving have been estimated at 0.14 and 140°, respectively, using Figures 11 and 12. As before, the relationship between ϕ and Δ_s approximates the simulation results well.

With an extremely simplified approach, we have determined the relationship between the radial Poynting vector and the phase shift between u_x and b_z. This proves that either can be used as a definitive measure of the end of the driving period: either through a change in the ratio of inward to outward signal of S_x, i.e.,

returning to a standing mode or through the phase shift returning to 90°. This idea can be extended to considering a more physical model of an inward propagating wave with a smaller amplitude reflected wave, expressed as follows (in normalized units):

$$u_x = \cos(\omega t + k_x x - k_y y)\cos(k_z z) + R\cos(\omega t - k_x x - k_y y)\cos(k_z z), \tag{8}$$

for $-1 < R < 1$, where R is the amplitude of the reflected wave, ω the frequency, and k_x, k_y, and k_z the wave numbers in the x, y, and z directions, respectively. Using equations (1) and (4) with the z dependence stated explicitly, we can calculate b_z given as

$$b_z = -A\cos(\omega t + k_x x - k_y y)\cos(k_z z) + AR\cos(\omega t - k_x x - k_y y)\cos(k_z z), \tag{9}$$

where

$$A = \frac{\rho\omega}{k_x} - \frac{k_z^2}{\omega k_x}.$$

and $\omega^2 = V_A^2\left(k_x^2 + k_y^2 + k_z^2\right)$. For the location of THD, we assume $k_y \approx 0$ by the close proximity to the symmetry line of the driver, and $z = 0$ by the small magnetic latitude (~3°). With this, equations (8) and (9) become

$$u_x = \cos(\omega t + k_x x) + R\cos(\omega t - k_x x), \tag{10}$$

$$b_z = -A'\cos(\omega t + k_x x) + A'R\cos(\omega t - k_x x), \tag{11}$$

where $A' = k_x/\omega$. To determine the phase shift between these components, we express them as

$$u_x = G\cos(\omega t + \psi),$$
$$b_z = G'\cos(\omega t + \psi'),$$

with

$$G = \sqrt{1 + R^2 + 2R\cos(2k_x x)},$$
$$G' = -A'\sqrt{1 + R^2 - 2R\cos(2k_x x)},$$
$$\psi = \tan^{-1}\left(\frac{1-R}{1+R}\tan(k_x x)\right),$$
$$\psi' = \tan^{-1}\left(\frac{1+R}{1-R}\tan(k_x x)\right).$$

Hence, u_x and b_z can be written as

$$u_x = G\cos\left(\omega t + \tan^{-1}(\alpha\tan(k_x x))\right),$$
$$b_z = -G'\cos\left(\omega t + \pi + \tan^{-1}\left(\frac{1}{\alpha}\tan(k_x x)\right)\right),$$

where $\alpha = (1-R)/(1+R)$ and $-G'$ is positive. The phase is dependent on R, k_x, and the position in x. In order to calculate the phase difference ϕ between the components, we consider b_z to be leading, such that the difference is given by

$$\phi = \pi + \tan^{-1}\left(\frac{1}{\alpha}\tan(k_x x)\right) - \tan^{-1}(\alpha\tan(k_x x)) = \pi + \tan^{-1}\left(\frac{2R}{1-R^2}\sin(2k_x x)\right). \tag{12}$$

As in the simplified approach above, we calculate the ratio of inward to outward S_x. We first calculate S_x using equations (10) and (11) as

$$S_x = u_x b_z,$$
$$= -A'\cos^2(\omega t + k_x x) + R^2 A'\cos^2(\omega t - k_x x).$$

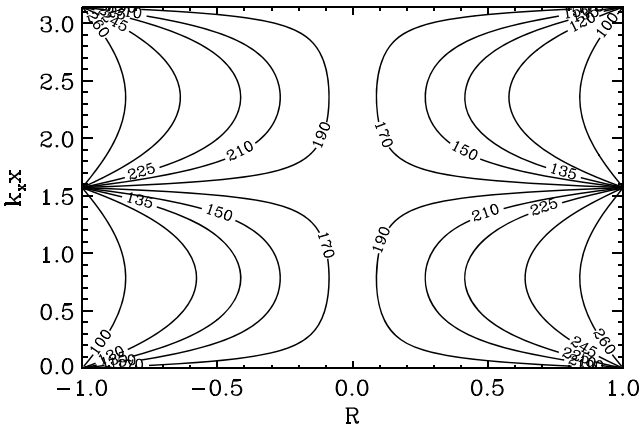

Figure 14. Contour plot of $\phi(k_x x, R)$, the phase by which b_z leads u_x, with labeled contours in degrees.

As previously, we seek to express S_x as a single sinusoidal function, which yields

$$S_x = \gamma + C \sin(2\omega t + \delta),$$

where

$$\gamma = R^2 - 1,$$
$$C = \sqrt{R^4 + 1 - 2R^2 \cos(4k_x x)},$$
$$\delta = \tan^{-1}\left(\frac{R^2 - 1}{\tan(2k_x x)(R^2 + 1)}\right),$$

and a constant factor of $A'/2$ has been removed which will not affect further analysis. Hence, the ratio of positive to negative signal Δ_s can be expressed as the maximum outward to the maximum inward Poynting vector as

$$\Delta_s = \left|\frac{R^2 - 1 + \sqrt{R^4 + 1 - 2R^2 \cos(4k_x x)}}{R^2 - 1 - \sqrt{R^4 + 1 - 2R^2 \cos(4k_x x)}}\right|, \tag{13}$$

given that the maximum and minimum of S_x will occur where $\sin(2\omega t + \delta) = \pm 1$.

The functions ϕ and Δ_s contain the necessary information to link the phase by which b_z leads u_x and the radial Poynting vector ratio. Figure 14 shows a contour plot of ϕ in R-$k_x x$ space, where the value of the reflection coefficient R is defined over $[-1, 1]$, while $k_x x$ is defined over $[0, \pi]$. This ensures that all possible solutions are considered since ϕ is periodic over π by virtue of the $\sin(2k_x x)$ term appearing in (12). The contours are labeled in degrees which highlights the symmetry for phase shifts between $90° \rightarrow 180°$ and $180° \rightarrow 270°$. These contours allow the values of $k_x x$ and the reflection coefficient to be constrained. For example, considering a phase shift of 120° implies $0.6 < |R| < 1$, which reveals information about the strength of the reflection of the mode. The contours of Δ_s have been omitted since $\phi(k_x x, R)$ and $\Delta_s(k_x x, R)$ actually have the same contours in R-$k_x x$ space, despite being on first appearance two completely separate functions (see (12) and (13)). It can be proven whether these contours are in fact the same by considering the gradients of each function. If the gradients are parallel, this implies that the functions share the same contours and hence one can be expressed as a function of the other. In order to show that the gradients are parallel we require

$$\nabla\phi \times \nabla\Delta_s = 0,$$
$$\Rightarrow \frac{\partial\phi}{\partial R}\frac{\partial\Delta_s}{\partial(k_x x)} - \frac{\partial\phi}{\partial(k_x x)}\frac{\partial\Delta_s}{\partial R} = 0. \tag{14}$$

After some algebra, equation (14) can indeed be shown to be satisfied and hence $\phi = \phi(\Delta_s)$. This implies that each phase shift ϕ corresponds to a precise ratio of outward to inward radial Poynting vector Δ_s. This is the same conclusion that was determined by the simple analysis of two-phase-shifted sine waves. In plotting Δ_s as a function of ϕ for a fixed $k_x x$ we produce exactly the same plot as in Figure 13. It is, perhaps, surprising that such a plot does not depend upon the choice of $k_x x$. This implies that the relationship between ϕ and Δ_s is independent of nodal structure and position. The more rigorous analysis provided here, with the addition of a reflected component, provides a better comparison to a more physical situation but yields the same relationship between the phase shift and the radial Poynting vector as the simple case.

We have shown that the phase shift between u_x (E_y) and b_z is inextricably linked with the overall shape of the radial Poynting vector. The ratio between the positive and negative S_x signal determines on a continuous scale the phase by which b_z leads u_x, which ranges from 90° (or 270°) for equally inward and outward, to 180° for purely inward propagation. Figure 13 can be used to determine the validity of an observation as a global mode, i.e., if the observed phase shift and ratio of positive to negative radial Poynting vector are a valid pairing. The above analysis also confirms that the change in S_x from the driven to post driven phases

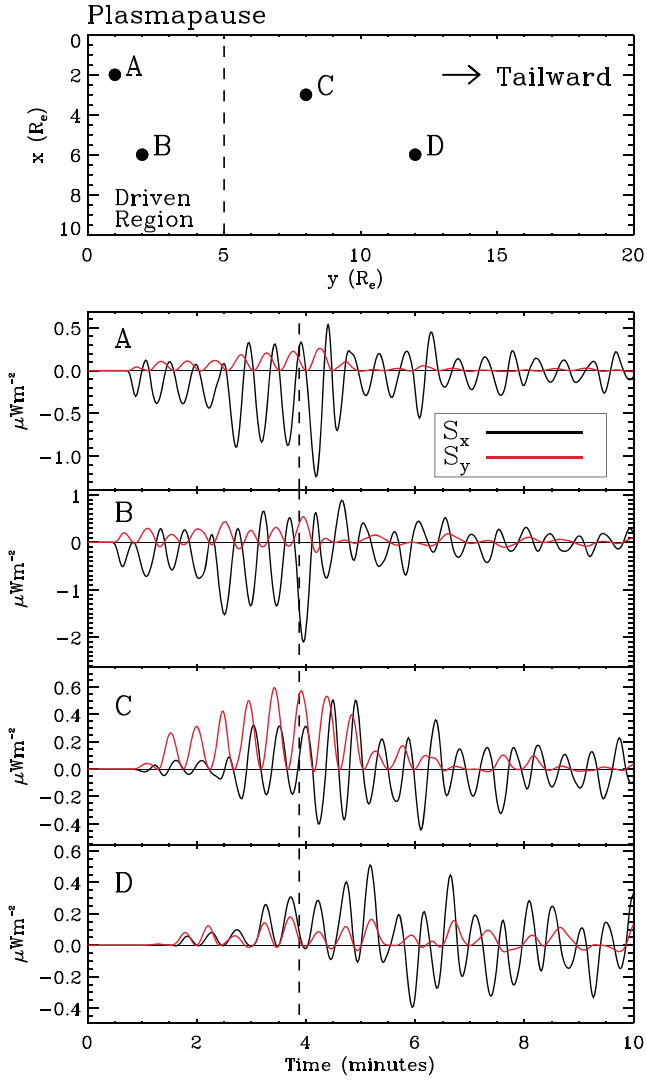

Figure 15. (top) The positions of four satellites placed in the model waveguide with the vertical dashed line indicating the driven region. (bottom four panels) The S_x (black) and S_y (red) plotted against time at the four satellite positions corresponding to those depicted in Figure 15, top.

correlates directly with the change in the phase shift. Hence, both the S_x signal and the phase shift can be used to clearly infer the end of the driving phase. For example, in the THD data in Figure 2, we can estimate that the driving stops at ~06:46 UT, where the phase changes to ~90° (fourth panel) and the radial Poynting vector recovers to an equally inward and outward signal (sixth panel).

6. Summary

The two simulations performed are very similar. In both cases, fast mode waves enter the domain through a disturbance in the compressional magnetic field component b_z. Most of the energy propagates first within the azimuthal extent of the driven region shown through S_x, with some energy leaking tailward through S_y. There is no resonance within the domain for either equilibrium as these points would exist beyond the inner boundary. Driving at the second radial harmonic eigenfrequency in each case precludes the appearance of other frequency modes, allowing the clear detection of the natural waveguide mode post driving in the compressional components. As mentioned separately in each of the discussion sections, the main influence on signal structure is the satellite location. Here we have investigated two very different signals that can be explained almost fully by the same simulation just by the positioning of the satellites.

To demonstrate this further, Figure 15 displays the radial and azimuthal Poynting vector components (S_x and S_y, respectively) plotted against time for four satellite locations in our model waveguide using the parameters from the Cluster simulation. The locations are shown as points A–D in Figure 15 (top), the coordinates of which are as follows: A($x = 2, y = 1$), B($x = 6, y = 2$), C($x = 3, y = 8$), and D($x = 6, y = 12$), with the z coordinate for all points being close to the magnetic equator at $z = 0.45$ (all lengths in R_E). The driver is the same as in the Cluster simulation given in Figures 5 and 6. In each of the plots, S_x is represented by the black line and S_y by the red line. The driven portion of the $x = 10\ R_E$ boundary extends to $y = 5\ R_E$, as shown by the vertical dashed line in Figure 15 (top). The vertical dashed line in the bottom four panels demarcates the time when the driver is switched off at $t = 3.88$ min. Position A corresponds to the location of the THEMIS satellite THD, and despite using the parameters for the Cluster simulation, the predominant features are the same: an inward radial Poynting vector during driving leveling out to an equally inward and outward signal post driving with a small positive azimuthal Poynting vector during the driven period. The fact that the signals match purely by positioning the satellite at the same point in the guide, shows the importance of the satellite location. Positions B–D show an interesting trend with satellite location. Consider first the radial Poynting vector S_x. During driving the signal changes from dominantly inward (negative) at B, to equally

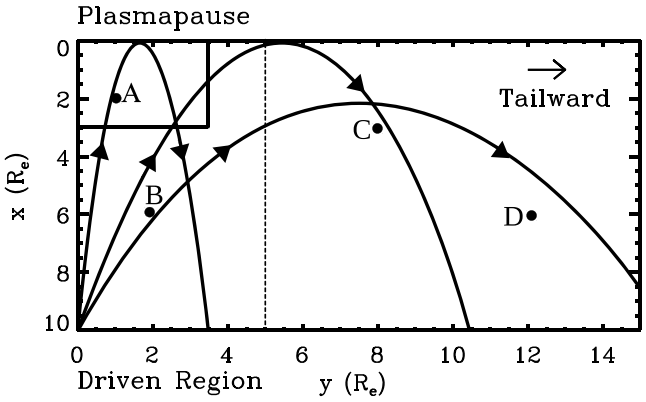

Figure 16. Waveguide schematic displaying possible ray trajectories.

back and forth at C, to mostly outward (positive) at D. We believe this progression can be best explained by ray trajectories, as shown in Figure 16. The trajectory depends upon the wave numbers in the $\hat{\mathbf{x}}$ and $\hat{\mathbf{y}}$ directions, namely, k_x and k_y. The driven extent in y suggests that a broad range of k_y modes will be excited, with amplitudes peaked at $k_y = 0$ and falling of at $k_y = 10$ [see *Rickard and Wright*, 1994]. Most of the energy is confined around the $k_y = 0$ modes and does not propagate to the locations C and D in Figure 15 during the simulation time. For the larger k_y modes, however, some energy propagates tailward and can have a turning point within the domain depending on k_y. We believe this to be responsible for the differing S_x signals. It is interesting to note that an outward radial Poynting vector signal can result at a location reasonably far down the magnetospheric flank purely from an upstream source during the driving phase, e.g., satellite D. The box outlined in the upper left corner of Figure 16 is purely to illustrate the directional flow of energy within the driving region close to the inner boundary as discussed in section 5.3. We see that there is energy flow radially inward and outward, with more rays entering radially. This is balanced by one ray exiting the azimuthal boundary.

The azimuthal Poynting vector also changes markedly with the movement of the satellites farther tailward. At B, within the driven region, S_y is small compared to S_x and is at times sunward (negative). This occurs due to the position within the driving region, where waves can emanate from the farthest azimuthal extent of this region ($y = 5\ R_E$) and travel sunward. At location C, S_y is more pronounced and purely tailward. This is a feature of the Cluster data caused by the movement of the satellite farther downtail. Finally at D, the signal is again purely tailward by nature of the farther downtail position. Considering post driving, there is a clear tendency for S_x to indicate a radial standing structure. Outside the driving region there is tailward propagation, while inside dispersion leaves only small k_y modes.

In this paper, we have modeled two ULF wave observations from the Cluster (*Clausen08*) and THEMIS (*Hartinger12*) satellites using a simple numerical waveguide model. We have developed a new boundary condition at the driven magnetopause that acts as a pressure driver (see Appendix A). The simulation results match favorably to the aforementioned observations and many interesting features may be discerned from the results.

1. The satellite position is of paramount importance in determining the structure of the signal observed. A location tailward of the disturbed region of the magnetopause will result in a purely tailward azimuthal Poynting vector, which explains the standout feature of the Cluster data. The location of the source region relative to the spacecraft can also be inferred from the Poynting vector components.
2. An overall inward radial Poynting vector signal does not necessarily require coupling to an FLR or a leaky inner boundary to explain the energy loss. The inward energy flow may be entirely balanced by tailward propagation, not immediately apparent from a perhaps small azimuthal Poynting vector signal. When a net inward energy flow does occur, the point where the signal returns to an equally back and forth oscillation demarcates the time when the driving stops.
3. The phase difference between the radial velocity (azimuthal electric field) and the field-aligned magnetic field can be used to infer whether the mode is propagating or standing radially and hence is another indicator of the transition between the driven and post driven phases.

These features of magnetospheric waveguide modes can be used to help interpret observational signatures.

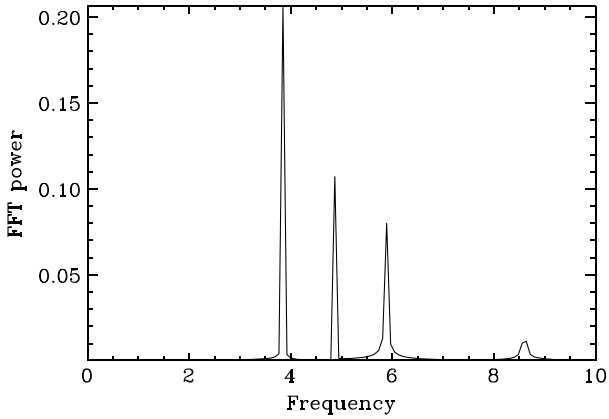

Figure A1. FFT for a uniform medium driven continuously at $\omega = 4.865$. The natural frequencies with a node of b_z at $x = 1$ are $\omega_1 = 3.85$, $\omega_2 = 5.88$, and $\omega_3 = 8.60$.

Appendix A: Analysis of Natural Waveguide Frequency With a b_z Driven Boundary

It is of interest to explain the new boundary condition, where the simulation is driven by perturbations in b_z as opposed to the radial displacement ξ_x or velocity u_x as in previous studies [e.g., *Rickard and Wright*, 1994; *Wright and Rickard*, 1995b], from which we can infer the radial nodal structure of the waveguide modes. In these studies, the inner boundary of the waveguide ($x = 0$) is perfectly reflecting with a node of u_x and driving with u_x at the outer boundary ($x = 1$ in dimensionless units), also simulates a node of u_x, resulting in a half wavelength fundamental mode. Our aim here is to demonstrate that driving with b_z simulates a node of b_z at the outer boundary, which together with an antinode of b_z at the inner boundary creates a quarter wavelength fundamental radial mode. This has been previously posited by *Mann et al.* [1999], who suggested that this boundary condition could lower the eigenfrequencies of the waveguide, without resorting to unrealistically large magnetospheric plasma densities.

The driving condition is implemented by overwriting the value of b_z on the $x = 1$ boundary. Throughout the computational domain, centered differences are used for the spatial derivatives, with ghost or halo cells used for the boundary calculations. On the driven boundary, however, centered differences cannot be implemented, since no information exists beyond the prescribed boundary value. Hence, for the derivatives in x ($\partial b_z/\partial x$ and $\partial u_x/\partial x$), fourth-order backward differencing is employed. In the predictor step of the leapfrog trapezoidal method [*Rickard and Wright*, 1994, equation (13)], the boundary value for b_z is overwritten by our prescribed (driven) value. The prescribed value is then used in the corrector steps [*Rickard and Wright*, 1994, equations (14)–(15)]. This implies that the resulting value is not in fact the desired driven boundary value as it has itself been changed through the corrector steps. To adjust this, b_z is once again overwritten with the previously prescribed boundary value.

In order to show the resulting nodal structure of the waveguide with this new boundary condition, we consider a uniform medium waveguide with fixed wave numbers in y and z, namely, k_y and k_z, respectively. If driving with the b_z perturbation acts as a node of b_z at the outer boundary as expected, then there is a quarter wavelength radially between $x = 0$ and $x = 1$, resulting in a dimensionless wavelength of 4 for the fundamental mode. The radial wave number k_x is then calculated simply through the relation $k_x = 2\pi/\lambda_x$. The fast mode dispersion relation can be used to determine the expected eigenfrequencies for the waveguide, given as

$$\omega^2 = V_A^2(k_x^2 + k_y^2 + k_z^2),$$

where the Alfvén speed is just 1 by virtue of the homogeneous waveguide. The wavelength of the second and third harmonics matching the boundary conditions are $\lambda_{x2} = 4/3$ and $\lambda_{x3} = 4/5$, respectively. This results in the radial wave numbers $k_{x1} = \pi/2$, $k_{x2} = 3\pi/2$, and $k_{x3} = 5\pi/2$. Inputting these values into the above dispersion relation, together with a choice of $k_y = \pi/2$ and $k_z = \pi$, yields the eigenfrequencies $\omega_1 = 3.85$, $\omega_2 = 5.88$, and $\omega_3 = 8.60$. If these frequencies can be reproduced from the simulation, it will then be clear that indeed the new boundary condition does enforce a quarter wavelength radial structure.

As a difference to the simulations previously discussed in sections 4 and 5, the $x = 1$ boundary is driven continuously over the full extent in the y direction. The driving frequency is chosen between the first and second harmonic frequencies as $\omega_d = 4.865$, such that no one frequency is dominantly driven. Figure A1 shows an FFT taken at a point near the middle of the domain in x, close to the $y = 0$ boundary. Three clear frequency peaks are visible, matching well to the predicted first and second harmonics and to the driving

frequency. A weak response is also observed around the predicted third harmonic frequency. This is clear evidence that driving the outer boundary with the b_z perturbation simulates a node of b_z, to give a quarter wavelength fundamental mode.

Acknowledgments
T.E. would like to thank STFC for financial support for a doctoral training grant. Data from simulation results are available on request from T. Elsden (email:te55@st-andrews.ac.uk).

Alan Rodger thanks the reviewers for their assistance in evaluating this paper.

References

Allan, W., E. M. Poulter, and S. P. White (1986a), Impulse-excited hydromagnetic cavity and field-line resonances in the magnetosphere, *Planet. Space Sci.*, *34*(4), 371–385, doi:10.1016/0032-0633(86)90144-3.

Allan, W., E. M. Poulter, and S. P. White (1986b), Hydromagnetic wave coupling in the magnetosphere: Plasmapause effects on impulse-excited resonances, *Planet. Space Sci.*, *34*(12), 1189–1200, doi:10.1016/0032-0633(86)90056-5.

Chen, L., and A. Hasegawa (1974), A theory of long-period magnetic pulsations: 1. Steady state excitation of field line resonance, *J. Geophys. Res.*, *79*(7), 1024–1032, doi:10.1029/JA079i007p01024.

Chi, P. J., and C. T. Russell (1998), Phase skipping and Poynting flux of continuous pulsations, *J. Geophys. Res.*, *103*(A12), 29,479–29,491, doi:10.1029/98JA02101.

Claudepierre, S. G., M. Wiltberger, S. R. Elkington, W. Lotko, and M. K. Hudson (2009), Magnetospheric cavity modes driven by solar wind dynamic pressure fluctuations, *Geophys. Res. Lett.*, *36*, L13101, doi:10.1029/2009GL039045.

Clausen, L. B. N., T. K. Yeoman, R. Behlke, and E. A. Lucek (2008), Multi-instrument observations of a large scale Pc4 pulsation, *Ann. Geophys.*, *26*, 185–199, doi:10.5194/angeo-26-185-2008.

Cummings, W. D., S. E. DeForest, and R. L. McPherron (1978), Measurements of the Poynting vector of standing hydromagnetic waves at geosynchronous orbit, *J. Geophys. Res.*, *83*(A2), 697–706, doi:10.1029/JA083iA02p00697.

Harrold, B. G., and J. C. Samson (1992), Standing ULF modes of the magnetosphere: A theory, *Geophys. Res. Lett.*, *19*(18), 1811–1814, doi:10.1029/92GL01802.

Hartinger, M., V. Angelopoulos, M. B. Moldwin, Y. Nishimura, D. L. Turner, K.-H. Glassmeier, M. G. Kivelson, J. Matzka, and C. Stolle (2012), Observations of a Pc5 global (cavity/waveguide) mode outside the plasmasphere by THEMIS, *J. Geophys. Res.*, *117*, A06202, doi:10.1029/2011JA017266.

Junginger, H. (1985), Poynting vector as a diagnostic of hydromagnetic wave structure, *J. Geophys. Res.*, *90*(A5), 4155–4163, doi:10.1029/JA090iA05p04155.

Kivelson, M. G., and D. J. Southwood (1985), Resonant ULF waves: A new interpretation, *Geophys. Res. Lett.*, *12*(1), 49–52, doi:10.1029/GL012i001p00049.

Kivelson, M. G., and D. J. Southwood (1986), Coupling of global magnetospheric MHD eigenmodes to field line resonances, *J. Geophys. Res.*, *91*(A4), 4345–4351, doi:10.1029/JA091iA04p04345.

Le, G., and C. T. Russell (1996), Solar wind control of upstream wave frequency, *J. Geophys. Res.*, *101*(A2), 2571–2576, doi:10.1029/95JA03151.

Lee, D. H., and R. L. Lysak (1989), Magnetospheric ULF wave coupling in the dipole model: The impulsive excitation, *J. Geophys. Res.*, *94*(A12), 17,097–17,103, doi:10.1029/JA094iA12p17097.

Mann, I. R., A. N. Wright, and P. S. Cally (1995), Coupling of magnetospheric cavity modes to field line resonances: A study of resonance widths, *J. Geophys. Res.*, *100*(A10), 19,441–19,456, doi:10.1029/95JA00820.

Mann, I. R., A. N. Wright, K. J. Mills, and V. M. Nakariakov (1999), Excitation of magnetospheric waveguide modes by magnetosheath flows, *J. Geophys. Res.*, *104*(A1), 333–353, doi:10.1029/1998JA900026.

Proehl, J. A., W. Lotko, I. Kouznetsov, and S. D. Geimer (2002), Ultralow-frequency magnetohydrodynamics in boundary-constrained geomagnetic flux coordinates, *J. Geophys. Res.*, *107*(A9), 1225, doi:10.1029/2001JA000135.

Rickard, G. J., and A. N. Wright (1994), Alfvén resonance excitation and fast wave propagation in magnetospheric waveguides, *J. Geophys. Res.*, *99*(A7), 13,455–13,464, doi:10.1029/94JA00674.

Rickard, G. J., and A. N. Wright (1995), ULF pulsations in a magnetospheric waveguide: Comparison of real and simulated satellite data, *J. Geophys. Res.*, *100*(A3), 3531–3537, doi:10.1029/94JA02935.

Southwood, D. J. (1974), Some features of field line resonances in the magnetosphere, *Planet. Space Sci.*, *22*(3), 483–491, doi:10.1016/0032-0633(74)90078-6.

Takahashi, K., and A. Y. Ukhorskiy (2008), Timing analysis of the relationship between solar wind parameters and geosynchronous Pc5 amplitude, *J. Geophys. Res.*, *113*, A12204, doi:10.1029/2008JA013327.

Waters, C. L., K. Takahashi, D.-H. Lee, and B. J. Anderson (2002), Detection of ultralow-frequency cavity modes using spacecraft data, *J. Geophys. Res.*, *107*(A10), 1284, doi:10.1029/2001JA000224.

Wright, A. N. (1994), Dispersion and wave coupling in inhomogeneous MHD waveguides, *J. Geophys. Res.*, *99*(A1), 159–167, doi:10.1029/93JA02206.

Wright, A. N., and G. J. Rickard (1995a), A numerical study of resonant absorption in a magnetohydrodynamic cavity driven by a broadband spectrum, *Astrophys. J.*, *444*, 458–470, doi:10.1086/175620.

Wright, A. N., and G. J. Rickard (1995b), ULF pulsations driven by magnetopause motions: Azimuthal phase characteristics, *J. Geophys. Res.*, *100*(A12), 23,703–23,710, doi:10.1029/95JA01765.